Journal Homepage: https://dergipark.org.tr/tr/pub/isibted

Isı Bilimi ve Tekniği Dergisi

Archive: https://tibtd.org.tr/dergi

Numerical Investigation of Three-Dimensional Fluid Flow and Heat Transfer from Finite Circular Cylinders in Tandem Arrangement

Tevfik Berker KOÇAK [1], Zekeriya ALTAÇ [1], Zerrin SERT [1, *]

[1] *Eskişehir Osmangazi University, Faculty of Engineering and Architecture, Mechanical Engineering, Odunpazarı, 26040, Eskişehir, Türkiye*

A R T I C L E I N F O

2026, vol.46, no.1, pp.141-155

doi: 10.47480/isibted.1813396

Research Article
Received: 30 October 2025
Accepted: 9 January 2026

* *Corresponding Author*
e-mail: zbocu@ogu.edu.tr

Keywords:
Computational fluid flow
External flow
Turbulent flow
Vortex structures
Wall-bounded flow

ORCID Numbers in author order:
0000-0002-7744-5492
0000-0001-9903-4427
0000-0001-6934-5443

A B S T R A C T

This study investigates the interplay between geometric spacing, thermal boundary conditions, and three-dimensional flow structures on heat transfer and aerodynamic performance in tandem finite circular cylinders. Two finite circular cylinders of diameter D and aspect ratio AR=3 placed vertically on the bottom wall (ground plane) of the computational domain are subjected to uniform external flow resulting in a Re=20000. The distance between the cylinders S was varied as S=D, 2D, 4D. The turbulence model SST k-ω is employed to solve the governing equations. First, a numerical verification study was conducted to determine the most suitable turbulence model and grid configuration using a single 3D cylinder for which benchmark data are available in the literature. Subsequently, the flow field is simulated for two cylinders arranged in a tandem configuration. As a significant new contribution to the literature, the primary turbulence and flow characteristics across the computational domain and on each cylinder surface are systematically identified and presented in tabular form. The heat transfer performance over isothermal cylinders is evaluated using the mean and local Nusselt number distributions, providing insights for design optimization. While no Kármán vortex street forms at S/D=1 due to irregular vortex shedding, a stable Kármán vortex street is observed at S/D=4. In terms of heat transfer, the highest performance is observed at S/D=1 for the upstream cylinder and at S/D=4 for the downstream cylinder. For the upstream cylinder, the average Nusselt number decreases by 13.9% from S/D=1 to S/D=2 and increases by 3.6% from S/D=2 to S/D=4. For the downstream cylinder, the average Nusselt number decreases by 12.6% from S/D=1 to S/D=2 and increases by 19.1% from S/D=2 to S/D=4.

Ard Arda Dizilimdeki Sonlu Dairesel Silindirlerden Üç Boyutlu Akış ve Isı Transferinin Sayısal İncelenmesi

M A K A L E B İ L G İ S İ

Anahtar Kelimeler:
Hesaplamalı akışkanlar akışı
Dış akış
Türbülanslı akış
Girdap yapıları
Duvarla sınırlı akış

Ö Z E T

Bu çalışma, tandem sonlu dairesel silindirlerde geometrik boşluk, ısıl sınır koşulları ve üç boyutlu akış yapıları arasındaki etkileşimin ısı transferi ve aerodinamik performans üzerindeki etkisini incelemektedir. Çapı D ve uzunluk/çap oranı AR=3 olan iki sonlu dairesel silindir, hesaplama alanın alt duvarında (zemin düzlemi) dikey olarak yerleştirilmiştir ve homojen dış akışa maruz bırakılmıştır. Bu akış, Re=20000 değerine ulaşmaktadır. Silindirler arasındaki mesafe S, sırasıyla S=D, 2D, 4D olarak değiştirilmiştir. Hesaplamalı akış denklemleri çözülmek üzere SST k–ω türbülans modeli kullanılmıştır. Öncelikle, literatürde mevcut referans verilerine sahip tek bir 3B silindir kullanılarak, en uygun türbülans modeli ve ağ yapılandırması belirlenmesi amacıyla bir sayısal doğrulama çalışması gerçekleştirilmiştir. Daha sonra, iki silindirin tandem konfigürasyonunda akış alanı simülasyonu yapılmıştır. Literatüre önemli bir yenilik olarak, hesaplama alanı boyunca ve her bir silindir yüzeyindeki temel türbülans ve akış özelliklerinin sistematik olarak belirlenip tablo halinde sunulması sağlanmıştır. İzotermal silindirler üzerindeki ısı transferi performansı, ortalama ve yerel Nusselt sayısı dağılımları kullanılarak değerlendirilmiş; tasarım optimizasyonu açısından öneriler sunulmuştur. S/D=1 durumunda düzensiz vorteks ayrışmaları nedeniyle Kármán vorteks caddesi oluşmamakta; ancak S/D=4 durumunda kararlı bir Kármán vorteks caddesi gözlenmektedir. Isı transferi açısından, yukarı akıştaki silindirde en yüksek performans S/D=1, aşağı akıştaki silindirde ise S/D=4 durumunda gözlenmiştir. Yukarı akış silindirinde, ortalama Nusselt sayısı S/D=1'den S/D=2'ye geçişte %13,9 azalırken, S/D=2'den S/D=4'e geçişte %3,6 artmıştır. Aşağı akış silindirinde ise, ortalama Nusselt sayısı S/D=1'den S/D=2'ye geçişte %12,6 azalırken, S/D=2'den S/D=4'e geçişte %19,1 artmıştır.

NOMENCLATURE

A	area
AR	aspect ratio
C_D	drag coefficient
CFD	computational fluid dynamics
d	diameter of small cylinder
D	diameter
D	dimension
DES	direct eddy simulation
F_D	drag force
f	frequency
H	height
$_{i,j,k}$	sub-indices
k	turbulence kinetic energy
L	length
LES	large eddy simulation
Nu	Nusselt number
P	perimeter
p	pressure
Pr	Prandtl number
Re	Reynolds number
S	distance between cylinders
St	Strouhal number
T	temperature
T_∞	inlet temperature
U_∞	inlet velocity
u,v,w	velocity components
x,y,z	direction components
β	blockage ratio
ω	turbulence dissipation rate
Θ	dimentionles temperature
τ	dimentionless time

INTRODUCTION

In engineering applications, unique geometries and component placement significantly influence the achievement of design objectives. From an engineering perspective, design considerations include mechanical strength, thermal management, performance, weight, cost, manufacturing process, material selection, availability, design flexibility, and operational safety. These criteria are evaluated and optimized to achieve specific design objectives. Finite cylinder structures, encountered in many applications, illustrate these principles. In large-scale applications include buildings and skyscrapers in metropolitan cities; medium-scale applications include industrial tanks, tubes, rooftop devices, and chimneys; small-scale applications include cooling systems (e.g., pin-fin cooling) and electronic components. An important aspect in the design of these products is the interplay between fluid mechanics and heat transfer. It is crucial to examine the flow and heat transfer characteristics in configurations involving finite cylinders and to incorporate these effects into the design process.

Cylinder structures, widely used in engineering applications, have also been researched extensively in the literature. Studies have extensively explored how these geometries affect flow patterns under uniform inlet conditions, varying velocity profiles, or oscillatory inlet flow. The vortex structures in such flows and their aerodynamic effects have been thoroughly examined in the literature using CFD simulations and experimental tests. Although the effects of geometric configuration and flow conditions on heat transfer have not been studied as thoroughly as flow dynamics, they remain of ongoing interest to researchers. Numerous two-dimensional numerical simulations, as well as three-dimensional numerical and experimental studies, have been conducted. Today, rather than focusing solely on theoretically examining various types of turbulence in flows, attention has shifted towards understanding the design implications of these turbulence structures. Despite technological advancements, two-dimensional assumptions from earlier studies continue to appear in the literature, whereas three-dimensional analyses, although increasingly common, have not yet matched the volume of research available for two-dimensional configurations.

In the literature, studies on heat transfer and fluid flow of cylinders with various cross-sections are mostly confined to two-dimensional analysis. Various researchers have studied infinite cylinders including; circular (Mahir and Altaç 2008; Zafar and Alam, 2019; Homsi et al., 2021), square (Sert et al., 2024; Göktepeli 2025b), rectangular (Zhang et al., 2022; Göktepeli 2025a), triangular (Altaç et al., 2019; Fallah et al., 2022; Çelik and Altaç, 2023; Sert, 2024), elliptical (Derakhshandeh and Gharib, 2021), semicircular (Yağmur et al., 2020), and other geometries. Hossain et al. (2021) investigated the mean pressure distribution around tandem square cylinders and the mean velocity distribution in their wake. They found that the critical gap should be four times the diameter of the cylinder (L/D=4) and observed negative drag coefficient on both cylinders at this critical gap. Alam et al. numerically studied flow, aerodynamic forces, and convective heat transfer for two tandem cylinders by varying the diameter ratio d/D=0.4–1.0 and spacing L/D=1.2–5.0 at Re=200. They found that larger d/D generally reduces mean drag, force fluctuations, and Nusselt number, while the spacing effect depends on whether the flow is in the reattachment or co-shedding regime; the critical spacing between these regimes varies non-monotonically with d/D, and peak local heat transfer occurs on the front surface linked to a near-wall velocity inflection point.

Among three-dimensional studies; Bangga et al. (2017) conducted analyses using the SST turbulence model on a three-dimensional finite circular cylinder. As a preliminary study, they performed a 2D analysis of an infinitely long circular cylinder, which demonstrated good agreement with experimental data. Upon examining the three-dimensional structure, they observed that the flow around the cylinder becomes three-dimensional at the base and interacts with the bottom wall. They were able to capture horseshoe vortices and other organized vortex structures. Krajnovic (2011) analyzed a finite circular cylinder at H/D=6 with Large Eddy Simulation (LES). His study observed that the vortex shedding region on the cylinder is consistent with previous research, with attached vortices from both sides. He identified two horseshoe vortices in the wake region, a large arch vortex extending from the top of the cylinder, and another vortex structure extending downward from the cylinder's downstream stagnation point. He found that the near-ground horseshoe vortex was unstable and could undergo sudden changes in shape. The time-averaged results showed the presence of three distinct horseshoe vortices, consistent with literature findings. He et al. (2017) determined that decreasing the H/D ratio in a finite cylinder structure resulted in a decrease in the drag coefficient C_D. They extensively examined the vortex structure formed at the free end of the cylinder. Using SST-DES (Shear Stress

Transport based Detached Eddy Simulation), they identified a vortex structure shedding downward from the rear end of the cylinder, accompanied by two parallel side vortices. Overall evaluations indicated reasonable agreement between tests and SST-DES simulations, demonstrating the method's suitability and economy for complex flows. Naik and Tiwari (2015) discovered that the wake length on a finite cylinder s strongly dependent on the Reynolds number, increasing with higher Reynolds numbers. Gouidmi et al. (2019) exposed a finite cylinder to a heat flux to investigate its effect on flow characteristics. Using the LES method, they placed a cylinder with H/D=5 on an adiabatic flat wall. They conducted repeated analyses of the velocity field and temperature distribution in three directions within the coordinate plane for cylinders of varying H/D, and the resulting Nusselt number distributions showed good agreement with experimental data.

Freidooni et al. (2021) conducted simulations to examine how urban ventilation and local wind patterns generated by city buildings affect pedestrian-level wind conditions. Focusing on the tandem arrangement of two rectangular-section cylinders, they considered two different aspect ratios (H/D=4 and 7), and spacing ratios of S/D= 1, 3, and 5. The flow regime significantly affects the pedestrian wind environment, with strong wind conditions occurring in small gaps and negligible wind speeds in vortex cores. In conclusion, they recommended a minimum value of S/D=3 to improve pedestrian wind comfort. Sharma et al. (2019) performed a computational analysis for the interaction between two square-shaped tall buildings (geometric ratio 1:1:7) arranged in tandem and exposed to turbulent atmospheric boundary layers. Helps mitigate adverse pedestrian wind conditions and suggested that the S/D ratio (gap/building width) should be at least 4. Kondo and Matsukuma (2005) conducted two-dimensional and three-dimensional analyses of tandem arrangements of cylinders using the third-order finite element method at Re=1000. Their study of aerodynamic forces revealed that the loads on the downstream cylinder were greater than those on the upstream cylinder. Additionally, they observed that the flow in the intermediate region and the vortex structures underwent abrupt changes when the spacing ratio between the two cylinders was approximately 3.5-4.

Studying three-dimensional flow and heat transfer over finite cylinders is crucial due to their relevance in a wide range of civil, structural, and environmental engineering applications. Structures such as chimneys, high-rise buildings, offshore risers, and tall towers are continuously subjected to atmospheric flows, and their finite height induces strong three-dimensional effects—such as tip vortices, span-wise flows, and complex wake structures—that are absent in idealized infinite-cylinder models. These three-dimensional flow phenomena directly influence aerodynamic forces, vortex-induced vibrations, and surface heat transfer rates, which are critical for structural safety and thermal management. In this regard, the present study investigates flow and heat transfer around tandem finite circular cylinders at Re=20000, a Reynolds number frequently used in two-cylinder flow studies because it provides a balance of rich, physically meaningful flow phenomena while remaining experimentally and numerically tractable. At Re=20000, the flow lies in the subcritical turbulent wake regime, where cylinder boundary layers are mostly laminar prior to separation, and the wake is fully turbulent with well-defined vortex shedding. This regime allows wake interference, vortex synchronization, shielding, and gap-flow effects between the cylinders to be strong, repeatable, and clearly observable. Despite extensive research on bluff bodies, systematic investigations of tandem finite circular cylinders under varying thermal conditions remain limited, particularly at Reynolds numbers where three-dimensional vortex dynamics dominate. While previous studies have considered single finite cylinders or tandem arrangements of square and rectangular cylinders, there remains a lack of comprehensive three-dimensional analyses of finite circular cylinders with AR=3 mounted on a ground plane under tandem configurations and varying thermal boundary conditions at Re=20000. This motivates the present work, which aims to provide detailed insights into both flow dynamics and heat transfer characteristics under realistic three-dimensional and thermal conditions.

The heat transfer characteristics of the downstream cylinder are governed primarily by the wake-induced flow structures generated by the upstream cylinder. The interaction between vortex shedding, velocity deficit, and enhanced turbulence intensity leads to significant modulation of the local thermal boundary layer. Furthermore, the finite length of the cylinders introduces strong three-dimensional effects, particularly near the end regions, which alter both the flow topology and the spatial distribution of the Nusselt number. For this reason, this study investigates the flow and heat transfer characteristics around two vertically arranged finite circular cylinders in tandem using three-dimensional computational fluid dynamics (CFD) simulations. The spacing between the cylinders was varied at S/D ratios of 1, 2, and 4. The cylinder closest to the inlet was called the “upstream cylinder” while the cylinder behind it was labeled the “downstream cylinder”. Furthermore, four distinct heating configurations were examined for each cylinder arrangement. The heating configurations comprised the following cases: (i) both cylinders were adiabatic (Case 1); (ii) the upstream cylinder was adiabatic whereas the downstream cylinder was isothermal (Case 2); (iii) the upstream cylinder was isothermal whereas the downstream cylinder was adiabatic (Case 3); and (iv) both cylinders were isothermal (Case 4). Numerical simulations were conducted for air at Pr=0.7 and Re=20000. Consequently, the flow and temperature fields were investigated, and the area averaged Nusselt numbers and time averaged local Nusselt numbers, together with the area averaged drag coefficients, were determined for each configuration.

PROBLEM DEFINITION AND MATHEMATICAL MODEL

Finite cylinders of D diameter and 3D height (AR=3) placed in tandem are subjected to a freestream with velocity U_∞ and temperature T_∞. The cylinders are located at the centerline of the flow domain in tandem configuration. It is assumed that finite cylinders are placed in the computational flow domain of $10D \times (35D+S) \times 6.5D$ dimensions. To prevent interference from the flow over the cylinders, the flow domain is bounded by an additional height of 3.5D above the cylinder free ends (He et al., 2017). The three-dimensional unsteady CFD analysis examines heat transfer and fluid characteristics. The study investigates three different distances between the cylinders: S=D, 2D, and 4D. The schematic of the physical problem addressed in this study is shown in Figure 1. The working fluid is air (Pr=0.7). The Reynolds number Re=20000 is selected to represent a moderately high flow regime where vortex shedding and unsteady flow phenomena are clearly developed, yet remain computationally feasible for 3D simulations. Since

the Reynolds number is more significant than 150, the turbulent flow exhibits three-dimensional characteristics, necessitating a three-dimensional analysis of the problem (Saha et al., 2003; Bangga et al., 2017; Liakos and Malamataris, 2016). This Reynolds is within the range commonly used in studies of tandem cylinder flows (Zhang et al., 2021), enabling meaningful comparison with existing literature while capturing the essential physics of wake interaction and heat transfer enhancement.

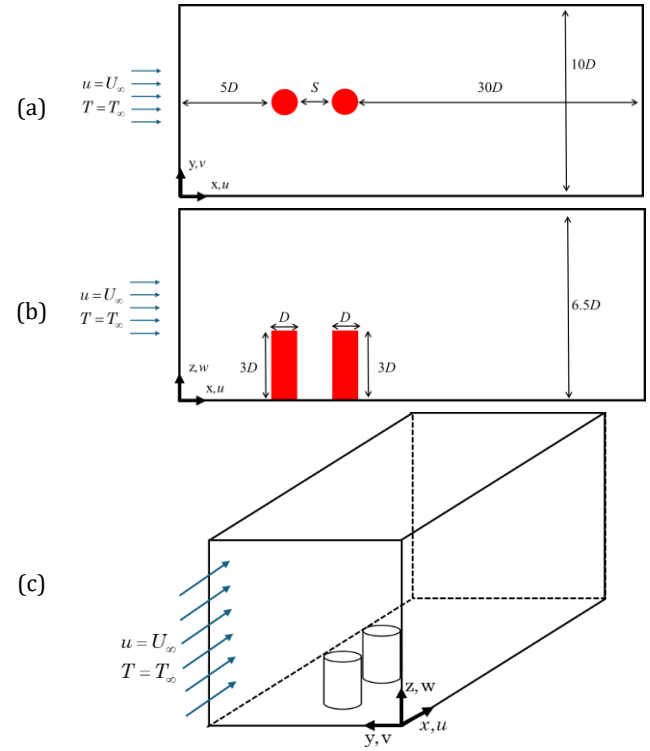

Figure 1. (a) Top view, (b) side view and (c) 3D view of the computational flow domain.

The unsteady governing dimensionless flow and energy equations for incompressible fluids can be expressed as follows (Zhang et al., 2021)

$$\frac{\partial \bar{u}_i}{\partial x_i} = 0 \tag{1}$$

$$\frac{\partial \bar{u}_i}{\partial t} + \frac{\partial}{\partial x_j}\left(\bar{u}_i\bar{u}_j + \overline{u_i'u_j'}\right) = -\frac{1}{\rho}\frac{\partial \bar{p}}{\partial x_i} + \frac{\partial \bar{\tau}_{ij}}{\partial x_j} \tag{2}$$

sub-indices i and j denote the components, respectively. u and p represent the time-averaged velocity and pressure fields, respectively. t denotes time, ρ is the density of the liquid (defined as a constant in this study), $\tau_{ij}=2\nu S_{ij}=\nu(\partial u_i/\partial x_j+\partial u_j/\partial x_i)$ is the time-averaged viscous stress tensor, $S_{ij}=(\partial u_i/\partial x_j+\partial u_j/\partial x_i)/2$ is the time-averaged strain tensor, and ν is the kinematic viscosity of the fluid. The introduction of the Reynolds stress tensor term (i.e., $T_{ij}=-u'_iu'_j$) makes this system explicit, and its closure requires a turbulence model. In this study, the Boussinesq vorticity-viscosity hypothesis is adopted, which states that:

$$\bar{T}_{ij} = -\overline{u_i'u_j'} = \upsilon_t\left(\frac{\partial \bar{u}_i}{\partial x_j} + \frac{\partial \bar{u}_j}{\partial x_i}\right) - \frac{2}{3}k\delta_{ij} \tag{3}$$

$$k = \frac{1}{2}\overline{u_i'u_j'} = \frac{1}{2}\left(\overline{u_x'u_x'} + \overline{u_y'u_y'} + \overline{u_z'u_z'}\right) \tag{4}$$

here k is the turbulent kinetic energy, δ_{ij} is the Kronecker delta symbol and υ_t is the turbulent viscosity of the flow.

Considering that strong pressure gradients and flow separation phenomena exist in the flow field scenario around a surface-mounted finite cylinder, the k-ω SST model (SST-V2003) developed by Menter et al. (2003) was used to obtain the turbulent viscosity υ_t.

$$\upsilon_t = \frac{\alpha_1 k}{max(\alpha_1\omega, SF_2)}; S = \sqrt{2S_{ij}S_{ij}};$$
$$F_2 = tanh\left[\left[max\left(\frac{2\sqrt{k}}{\beta\times\omega y}, \frac{500\upsilon}{y^2\omega}\right)\right]^2\right] \tag{5}$$

$$\frac{\partial k}{\partial t} = \frac{\partial(u_j k)}{\partial x_j} = \tilde{P}_k - \beta\times k\omega + \frac{\partial}{\partial x_j}\left[(\upsilon + \sigma_k\upsilon_t)\frac{\partial k}{\partial x_j}\right] \tag{6}$$

$$\frac{\partial \omega}{\partial t} + \frac{\partial(u_j\omega)}{\partial x_j} = \frac{\alpha\tilde{P}_k}{\upsilon_t} - \beta\omega^2 + \frac{\partial}{\partial x_j}\left[(\upsilon + \sigma_\omega\upsilon_t)\frac{\partial \omega}{\partial x_j}\right] + 2(1-F_1)\sigma_{\omega 2}\frac{1}{\omega}\frac{\partial k}{\partial x_j}\frac{\partial \omega}{\partial x_j} \tag{7}$$

where ω is the specific dissipation rate, S is the invariant measure of the deformation rate, P indicates the limited value of the k production term and is used here to prevent turbulence accumulation in stagnant regions using a production limiter.

$$F_1 = tanh\left\{\left\{min\left[max\left(\frac{\sqrt{k}}{\beta\times\omega y}, \frac{500\upsilon}{y^2\omega}\right), \frac{4\rho\sigma_{\omega 2}k}{CD_{k\omega}y^2}\right]\right\}^4\right\} \tag{8}$$

$$CD_{k\omega} = max\left(2\rho\sigma_{\omega 2}\frac{1}{\omega}\frac{\partial k}{\partial x_i}\frac{\partial \omega}{\partial x_i}, 10^{-10}\right) \tag{9}$$

$$\tilde{P}_k = min(P_k, 10\beta k\omega), P_k = \upsilon_t\frac{\partial \bar{u}_i}{\partial x_j}\left(\frac{\partial \bar{u}_i}{\partial x_j} + \frac{\partial \bar{u}_j}{\partial x_i}\right) \tag{10}$$

The boundary conditions suitable for the physical problem need to be prescribed to solve the governing equations.

- **Initial condition:** The fluid is assumed to be at rest (u=v=w=0 for t<0), and the transient flow simulation is activated by prescribing the inlet condition at t=0.
- **Inlet:** The flow enters the environment perpendicularly with a uniform speed and density; i.e., the freestream velocity components at the inlet are prescribed as u=U_∞, v=0, and w=0. The inlet fluid temperature is uniform, i.e., T=T_∞. The turbulence intensity was defined as 0.5%, and the length scale ratio was defined as 0.551 for AR=3.
- **Bottom Wall:** A no-slip boundary condition (u=0, v=0, and w=0) was applied to the bottom wall, which is also kept as adiabatic$\left(\frac{\partial T}{\partial z}=0\right)$ in heat transfer simulations.
- **Cylinder Surfaces:** No-slip boundary conditions (u=0, v=0, and w=0) were also applied to the cylinders' free end and side walls. Isothermal surface temperature is prescribed to the walls of the heated cylinders, i.e., T=T_w. However, to determine the effect and interaction of the thermal boundary conditions (prescribed on the heated/unheated cylinders) on the heat transfer characteristics, four scenarios presented in Table 1 are also analyzed.

Table 1. Thermal boundary condition scenarios.

Case No	Upstream Cylinder Thermal BC	Downstream Cylinder Thermal BC
Case 1	adiabatic	adiabatic
Case 2	adiabatic	isothermal
Case 3	isothermal	adiabatic
Case 4	isothermal	isothermal

- **Side and Top Walls:** The side and top walls of the computational domain are defined parallel to the inlet (freestream) to reflect the external flow conditions; that is, $u=U_\infty$, $v=0$, $w=0$, and $T=T_\infty$.
- **Outlet:** It is defined as outflow, assuming that the fluid leaves the outlet surface; that is, $\frac{\partial u}{\partial x}=\frac{\partial u}{\partial x}=\frac{\partial w}{\partial x}=\frac{\partial T}{\partial x}=0$

The drag coefficient in terms of net aerodynamic load is as follows

$$C_D=\frac{2F_D}{\rho U_\infty^2 A} and\ F_D=\iint(-pn_x+(\tau\cdot n)_x)dA_s \quad (11)$$

where U_∞, is the freestream velocity, ρ is the fluid density, A is the projected area ($H\times D$), F_D is the friction force, p is the pressure, n_x is the x-component of the surface normal, A_s is the cylinder surface area, and $(\tau\cdot n)_x$ the x-component of viscous force. The Strouhal number (St), a dimensionless number, is used in fluid dynamics to characterize the flow of fluid around a body or an obstruction, and it is defined as follows:

$$St=\frac{fD}{U_\infty} \quad (12)$$

where D is the cylinder diameter and f is the oscillation frequency. In this study, the effects of flow characteristics on heat transfer are examined *via* the mean Nusselt number, a dimensionless heat transfer parameter, which is defined as

$$Nu=\frac{hD}{k}\ and\ h=\frac{1}{A_S}\iint h_{\theta,z}dA_s\,, h_{\theta,z}=\frac{q''(\theta,z)}{T_S(\theta,z)-T_\infty} \quad (13)$$

where h is the mean heat transfer coefficient, $h_{\theta,z}$is the local heat transfer coefficient on a cylinder surface, k is the thermal conductivity of the fluid, and D is the diameter (characteristic length). The local heat transfer coefficient in Eq. (13) is determined from the conductive flux at each surface node, and the mean coefficient is computed by taking the area-weighted average of these local values.

PROBLEM DEFINITION AND MATHEMATICAL MODEL

Numerical method

The governing flow and energy equations were solved using ANSYS 2019-R1-FLUENT, a Computational Fluid Dynamics (CFD) software based on the Finite Volume Method (FVM). The numerical solutions were obtained with the SIMPLE algorithm, which handles pressure-velocity coupling. A second-order upwind scheme is applied to differencing the convective terms (pressure, momentum, turbulent kinetic energy, specific dissipation rate and energy). A transient approach was applied within a pressure-based solution algorithm. For turbulence modeling, the SST k-ω model under URANS (Unsteady Reynolds-Averaged Navier-Stokes) was chosen based on literature research for suitability to the problem and computational resources. Previous numerical investigations of similar configurations in the literature provide strong justification for our choice. He (2017) employed the DES-SST model in their study, noting that the model operates in SST mode near walls and transitions to LES behavior in the bulk flow, thereby functioning as a hybrid turbulence modeling approach. They reported good agreement between their numerical results and experimental data. Zhang (2017) conducted their investigation at a relatively lower Reynolds number (Re=20000) compared to previous studies, and performed a comprehensive comparison using eight different RANS models and two LES models. Similar to He (2017), Zhang concluded that the SST k-ω model offered a more favorable balance between computational cost and accuracy, and thus recommended its use. Zhang et al. (2021) extended the work of Zhang (2017) by conducting a detailed parametric study encompassing geometry variations, boundary conditions, flow-influencing parameters, and different aspect ratios, again utilizing the SST k-ω model. Their results demonstrated strong agreement with experimental data.

Residual convergence criteria was set to 10^{-6} for continuity, momentum, turbulence, and energy equations. To ensure solution convergence, the mean velocity as well as the Nusselt number and drag coefficients on the upstream and downstream cylinders were continuously monitored. The simulation was continued for a minimum of 200 additional time steps to ensure that both the flow and heat transfer solutions were fully developed, and that the oscillatory behavior on the cylinders had stabilized and exhibited periodic, repeatable patterns over at least 10 observed periods, thereby confirming convergence. Time step size is 0.05 and maximum iterations per time step is 20. The SST k-ω turbulence model does not require a specific wall function but for resolving the boundary layer and heat transfer around surfaces the near wall mesh structure modeled as y+<5. A localized mesh refinement was employed to accurately capture the flow structures in critical regions, including the flow domain centerline, the cylinder surfaces and their immediate vicinity, the inter-cylinder gap, the wake regions downstream of the cylinders, and the downstream extension of the domain where Kármán vortex shedding develops. To resolve the boundary layer accurately, a specialized inflation layer was applied near wall surfaces, enabling effective control of the y+ values and ensuring reliable near-wall resolution.

The blockage ratio is determined by the inlet cross-sectional area (A) to the cylinder cross-sectional area (A_c) ratio. Zhang et al. (2021) state that the maximum blockage ratio should be less than 6% to avoid adverse effects on flow characteristics. The blockage ratio is calculated using the following;

$$\beta=\frac{A}{A_c}\times 100 \quad (14)$$

Additionally, the inlet cross-sectional area was set to extend 3.5D above the cylinder's free end to minimize its influence on the flow domain (He et al., 2017). The cylinders in the study have a 3D length. Therefore, the channel height was set as 6.5D (i.e., 3D+3.5D). As a result, the channel geometry was established with dimensions of 10D × (35D+S) × 6.5D.

The turbulence intensity and length scale are found analytically in the SST k-ω solution used for the external flow to determine the compatible k and ω values in the first iteration. They are assigned to the numerical calculations as the initial value. The turbulence intensity was accepted as 0.005 (0.5%), and the length scale was calculated as follows (Zhang et al., 2021).

$$k=\frac{3}{2}(U.l)^2 \quad (15)$$

$$\omega=C^{\frac{1}{4}}\frac{\sqrt{k}}{l} \quad (16)$$

$$l=0.07dh \quad (17)$$

$$dh=\left(\frac{4A}{P}\right) \quad (18)$$

where k is turbulence kinetic energy, ω is turbulence diffusion rate, u=U_∞, I=0.005, and C is turbulence model coefficient 0.09. The specific values for geometric parameters are presented in Table 2.

Table 2. Blockage ratio and length scale

AR	Blockage Ratio	Length Scale
3	4.6%	0.551

The governing equations are non-dimensionalized as follows:

$$(\bar{x},\bar{y},\bar{z}) = \frac{(x,y,z)}{D}, \tau = \frac{tU_\infty}{D}, U = \frac{u}{U_\infty}, \Theta = \frac{T-T_\infty}{T_w-T_\infty} \quad (19)$$

where $\bar{x},\bar{y},\bar{z}$ denote the dimensionless space, τ is the dimensionless time, U is the dimensionless velocity and Θ is the dimensionless temperature. Within the scope of the study, a time dependency analysis was performed with 0.1, 0.05 and 0.025 time intervals for tandem arrangement S/D=4 Case-4, as shown in Table 3. The subscripts 1 and 2 denote the upstream and downstream cylinders, respectively. The local Nusselt number, drag coefficient data on the cylinders, and the evolution of turbulent flow structures in the flow domain were systematically examined. The results obtained at each time interval were compiled and correlated with the corresponding computational run time. It was observed that further reduction in the time step size did not result in significant changes in the solution, indicating convergence. Although no major change in the general flow structure was observed, the time step size yielding the C_D and Nusselt number for both cylinders $d\tau = 0.05$ was selected, considering the computational efficiency and analysis duration. In general, when the flow time reaches $\tau \cong 120-130$ the flow regime is established and the solution is continued until $\tau \cong 200$ to ensure a stable or periodic flow is achieved.

Table 3. Time dependency analysis results: time-averaged drag and Nusselt numbers for S/D=4, Case-4

Time Interval	$C_{D,1}$	$C_{D,2}$	Nu_1	Nu_2
0.025	0.703	0.375	95.05	104.73
0.05	0.703	0.382	95.06	104.68
0.1	0.703	0.386	95.06	104.58

Verification

He et al. (2017), Zhang (2017), Zhang et al. (2021) applied O-grid around the cylinder and revealed a regular structure in the transitions. Zhang et al. (2021) included the flow over a finite circular cylinder and experimental verification, which was used as a reference in our study. Unlike researchers who use more than 9 million elements in their studies, we made the mesh structure more efficient in the specific regions, allowing the solver power to be used more efficiently.

It is observed that the channel width was selected as $22D$, and the channel height was selected as $15D$ height in the reference study. Additionally, a very wide octagonal geometry slicing around the cylinder was created, and this dense mesh structure was swept upward along the $15D$. It appears that the mesh can be produced more efficiently with much fewer elements. As a result of the literature research, control volume dimensions can be determined as the height of $3.5D$ from the free end of the cylinder is sufficient (He et al., 2017), and the channel width is enough to be less than 6% blockage ratio (Zhang et al., 2021). It has been understood that such a dense mesh used in unnecessary areas, which is far away from the cylinder free end and sideways will not affect the flow structure.

Considering the aspects that are open to improvement mentioned above, the control volume dimensions (width and height) and mesh structure were selected efficiently with literature data. A secondary square-shaped volume was defined around cylinders to create a local mesh and this volume was filled with uniformly distributed rectangular prism elements (structured mesh). In this mesh structure, the growth ratio was kept at 10% and the regions that have secondary importance for the flow solution were cleared of the local dense mesh structure and fewer elements were placed more efficiently. Figure 2 shows the mesh structure.

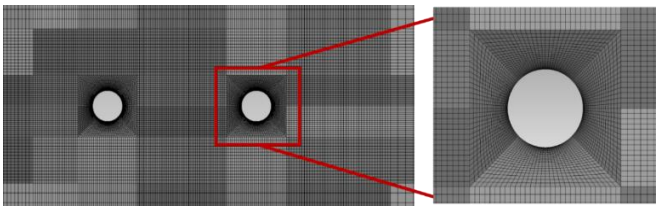

(a)

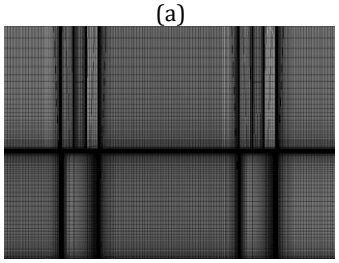

(b)

Figure 2. Mesh structure created on tandem cylinders a) z/D=2, b) xz center plane.

Within the scope of the verification study, different parameters on a single cylinder were analyzed, interpreted and compared with literature results. In this way, a reliable method has been presented for analyses to be carried out in the future stages.

The numerical simulations performed during the verification phase are presented in Table 4. Three different height-to-diameter ratios (AR), three different mesh densities, and three different downstream distances were examined and compared with the reference study. It was decided to use the mesh structure in the configuration V6 with AR=3 and 3.6M elements, which has a 2.3% difference from the reference study. In addition, by examining V1-V2-V3, it was determined that downstream length did not significantly change the friction coefficient. On the other hand, the flow structure in the wake region after the downstream cylinder can be observed more clearly with a distance of $30D$.

Table 4. Verification study analysis matrix

No	H/D	Down-stream Length	Elem. Num.	C_D (this study)	C_D (Zhang et al., 2021)	Delta
V1	2	$10D$	3.6 M	0.700	0.675	+%3.7
V2	2	$20D$	3.6 M	0.701	0.675	+%3.8
V3	2	$30D$	3.6 M	0.703	0.675	+%4.1
V4	2	$20D$	2.7 M	0.558	0.675	-%17.4
V5	2	$20D$	4.9 M	0.698	0.675	+%3.4
V6	3	$20D$	3.6 M	0.723	0.707	+%2.3
V7	4	$20D$	3.6 M	0.752	0.734	+%2.4

Following the verification study, a tandem cylinder structure was designed. In line with the experience gained in the flow volume mesh structure for verification study, a uniformly distributed mesh was created around the 1D diameter cylinders. A dense mesh structure was made again with a 10% growth rate preserved in the flow domain. It includes a secondary local dense mesh structure volume to capture turbulence around the cylinders and flow domain. Figure 3 shows the mesh structure of the bottom wall and the cylinders.

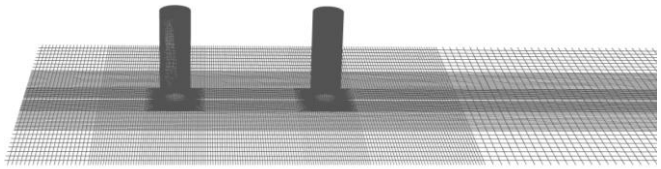

Figure 3. Cylinders and the mesh structure on the bottom wall.

The tandem flow analysis matrix and the obtained data are summarized in Table 5. H is the height of the cylinder, and subscripts 1 and 2 denote the upstream and downstream cylinders, respectively. An additional mesh convergence study was conducted for the tandem configuration at S/D =4, Case-4. Three mesh levels were tested: 2.8M, 3.6M, and 4.4M elements. The relative differences in time-averaged drag coefficient between the medium and fine meshes were below 1.2%, confirming mesh independence. Therefore, the medium mesh configuration was adopted for all tandem simulations. For varying spacing ratios, the influence of the wake of the upstream cylinder becomes evident. At a distance of 4D, the wake of the upstream cylinder results in a higher drag coefficient (C_D) on the downstream cylinder compared to other configurations.

In the downstream flow, a well-developed wake forms, consistent with the findings of Zhou and Yiu (2006). As the distance between cylinders decreases, the downstream cylinder's drag coefficient (C_D) decreases dramatically because it enters the near wake of the upstream cylinder. However, as the cylinders are brought closer together, the intermediate region becomes increasingly chaotic, resulting in fluctuations in C_D. This phenomenon is consistent with findings from the studies performed by Kondo and Matsukuma (2005), Zhou and Yiu (2006), Mahir and Altaç (2008), Sharma et al. (2019), and Zobeyer et al. (2021). Upon analyzing the flow structures within the scope of this study, it is observed that at S/D= 1, the Strouhal number reaches 0.136 on the upstream cylinder; however, no stable flow oscillation is detected on the downstream cylinder. At S/D= 2, flow oscillations are damped throughout the flow domain, and no distinct Strouhal number is observed. Finally, at S/D= 4, a well-developed Kármán vortex street forms downstream, resulting in a Strouhal number of 0.293 on the downstream cylinder.

Table 5. Mesh dependency and simulation results of tandem cylinders of the same length.

H_1/H_2	S/D	Elem. Num.	$C_{D,1}$	$C_{D,2}$	St_1	St_2	$\frac{\lvert U\rvert_{max}}{U_\infty}$
1	4	Coarse	0.721	0.256	-	0.292	1.36
1	4	Medium	0.703	0.384	-	0.293	1.36
1	4	Fine	0.698	0.388	-	0.293	1.36
1	1	Medium	0.802	0.210	0.136	-	1.51
1	2	Medium	0.697	0.104	-	-	1.36
1	4	Medium	0.703	0.384	-	0.293	1.36

RESULTS AND DISCUSSION

Following the modeling and verification study on a single cylinder, fluid flow and heat transfer analyses were conducted for tandem cylinder configurations. Two cylinders of AR=3 were arranged at distances S/D=1, 2, and 4. The vortex structures were observed, compiled, and presented in Table 6. Additionally, four different cylinder heating scenarios were considered (*see* Table 1), and the mean Nusselt number values were obtained. The effects of fluid flow on heat transfer over the cylinders were evaluated and explained in the heat transfer characteristics section.

Flow Structures

The flow over the circular cylinder's free end and flow around the cylinder- bottom wall junction cause the local flow field and the cylinder's wake to become strongly three-dimensional. The flow interactions with a finite cylinder, the resulting flow separations and vortex structures have been generally standardized in the literature. Kawamura et al. (1984) performed a flow visualization test, and classified these vortex structures. Sumner (2013) reviewed the research and published a good literature summary for the flow characteristic. Familiar vortex types are the Kármán vortex shedding (or boundary layer separation) from the sides of the cylinder, the horseshoe (or necklace) vortex forming upstream at the cylinder- bottom wall junction, and time-averaged stream wise counter-rotating vortex pairs within the wake, near the free end (the tip or trailing vortices) associated with a downwash flow on the wake centerline. Figure 4 schematically illustrates these vortex structures formed around a finite cylinder. In low aspect ratio cylinders (AR<2.5), the Kármán vortex structure is not expected (Sumner, 2015).

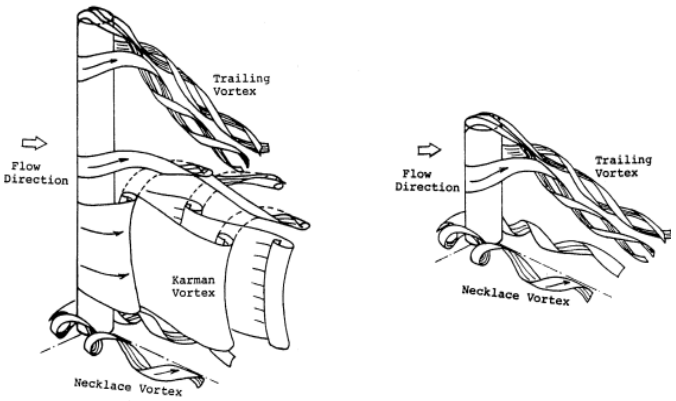

Figure 2. Vortex structures formed around a finite cylinder (Kawamura et al., 1984)

In a tandem arrangement, the flow and heat transfer from two cylinders of H/D=3 subjected to cross flow were investigated for S/D=1, 2, and 4. All cases investigated are classified and summarized in Table 6 concerning the flow structures observed. Seven distinct flow structures were identified and their respective structures on the cylinders were noted for each different cylinder spacing. This visualization helps us understand how the spacing between cylinders influences the flow characteristics, particularly the development of vortices and the vortex-shedding phenomenon.

Table 6. Classification of main flow characteristics in tandem cylinders.

Type	*S*/*D*=4		*S*/*D*=2		*S*/*D*=1	
	Upstream Cylinder	Downstream Cylinder	Upstream Cylinder	Downstream Cylinder	Upstream Cylinder	Downstream Cylinder
1. Kármán street	Continuous and growing		No Karman street development		No Karman street, scattered vorices	
2. Downstream characteristic	Wavy converging		Straight convrerging		Irregular converging	
3. Kármán vortex/ Boundary layer seperation	Straight symmetric	Shedding vortex	Straight returning	Straight symmetric	Narrow complex returning	Irregular shedding vortex
4. Horseshoe/Necklace vortex	Straight symmetric	Shedding vortex	Straight symmetric	Vortex and symmetric	Straight symmetric	Straight shedding
5. Tip boundary layer	Wide	Straight	Medium	Straight	Narrow	Straight
6. Trailing/Tip vortex	Wide returning	Wide returning and seperation	Medium returning	Medium turning and seperation	Narrow turning	Straight braid
7. Upwash	Far small upward	Near small upward	Large horizontal	Small horizontal	Small horizontal	Near large upward

As the distance between the cylinders differs, the vortex shedding development changes. For S/D=1, the vortex that comes from the upstream cylinder cannot create a fully developed shedding on the downstream cylinder. While in the case of S/D=4, it has enough distance to develop regular formation. The vortex shedding phenomenon for the S/D=4 case is depicted in Figure 5. The flow separations from the sides of the upstream cylinder led to Kármán vortices. As the flow interacts with the downstream cylinder, it generates a new vortex region in the wake of the downstream cylinder. Vortex shedding develops regularly and initiates the formation of Kármán street on the downstream cylinder, which is observable in the flow field (Type 3, S/D=4 in Table 6 as shown in Figure 5).

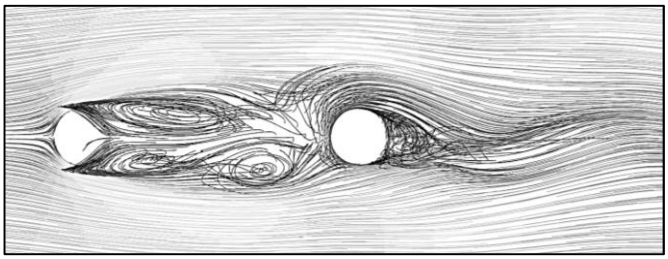

Figure 5. Streamlines view over cylinders at z/D=2 for S/D=4.

The velocity iso-surface visualization of the flow field for S/D=4 is given in Figure 6. The Kármán Street development is observed in S/D=4 and this structure corresponds to Table 6, Type 1.

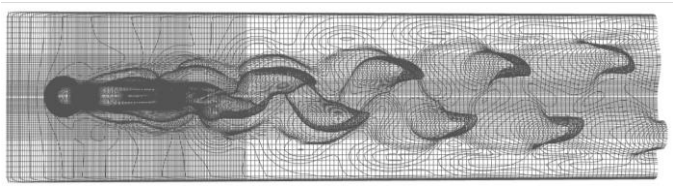

Figure 6. Kármán street development for S/D=4.

Figure 7 illustrates the velocity magnitude in the *xy* plane for z/D=2. As briefly summarized in Type 1 in Table 6, the fully developed Kármán Street is only observed in the S/D=4 arrangement. The street spreads out in the downstream direction. It is observed that the structure begins to become irregular, with small vortex breaks at the edges of the street and forms of large vortex islands downstream (Figure 7a). In the case of S/D=2, the development of the boundary layer on the downstream cylinder does not allow for the Kármán vortex to shed. This effect suppresses the development of a fully established Kármán Street, but a symmetrically expanding undisturbed flow field is observed in the downstream region (Figure 7b). In the case of S/D=1, the fluid flow expands irregularly in the downstream direction, with the vortices spreading and extending without any bounds (Figure 7c).

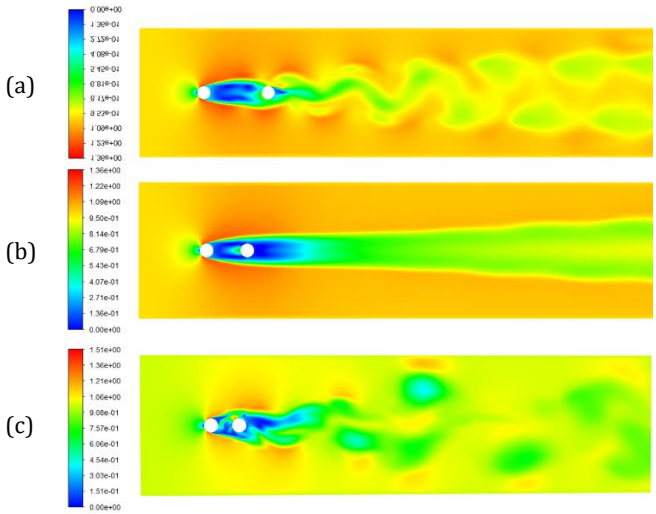

Figure 7. The dimensionless velocity magnitude in the *xy* plane at z/D=2 for (a) S/D=4, (b) S/D=2, and (c) S/D=1.

The velocity magnitude in the *xz* plane is illustrated in Figure 8. As shown in Type 2 in Table 6, the downstream regions of all arrangements have different characteristics. The effect of downwash that reduces the vertical extend of the wake can be seen in all cases. For S/D=4, the Kármán vortex shedding (Figure 7a) effects the central plane velocity distribution. The far wake flow of the downstream cylinder shows a vertical velocity distribution for each vortex shedding pass and converges to the bottom wall at the end of the control volume (Figure 8a). Due to S/D=2 showing a symmetrical flow character (Figure 7b), the wake region on the central plane also shows a uniformly distributed and converging flow field due to the downwash effect downstream (Figure 8b). Lastly, S/D=1 shows irregular and non-converged flow fields downstream (Figure 8c) due to chaotic and irregular vortex shedding over the cylinders (Figure 7c).

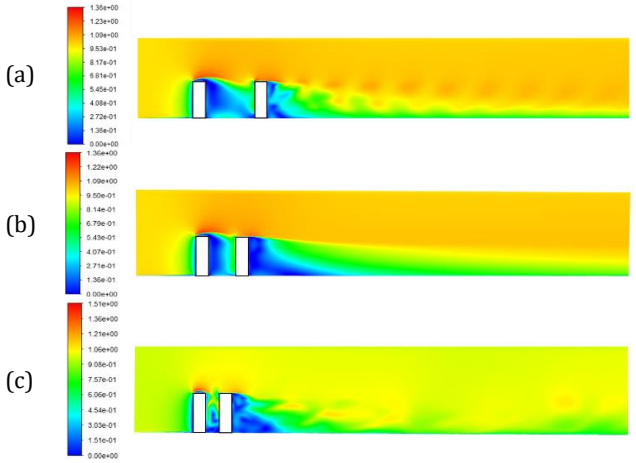

Figure 8. The dimensionless velocity magnitude in the *xz* plane at for a) S/D=4, b) S/D=2, and c) S/D=1.

Figure 9 shows the vorticity distribution for S/D=4. The flow leaving the cylinder side surfaces creates a structure that sheds vortices. These vortices initially have more or less the same height as the cylinders in the center plane (*xz*). Due to the downwash effect, they gradually lose strength and decrease height towards the bottom wall.

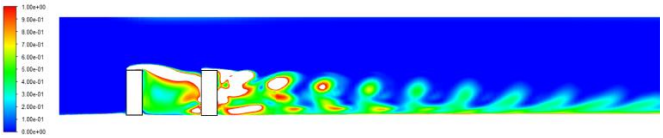

Figure 9. The vorticity distribution in the *xz* plane for S/D=4.

Figure 10 shows streamlines of downwash and Kármán vortex structure, which is a 3D combination of Figure 7 and Figure 8. As illustrated in Types 3 and 4 in Table 6, the upstream cylinder shows a symmetric Kármán and horseshoe vortex structure. However, the flow leaving the upstream cylinder becomes quite irregular in all cases as it interacts with the downstream cylinder. With the downwash effect, a recirculation zone occurs between the two cylinders. Especially in S/D=1 and 4, due to the vortex shedding the horseshoe vortex on the downstream cylinder is not symmetrical (Figure 10a and 10c). Unlike others, the horseshoe and Kármán vortex are symmetrical on both up and downstream cylinders in S/D=2. The flow lump occurring in the wake of upstream cylinder first connects to the downstream cylinder and then separates, forming a symmetrical horseshoe (Type 4, S/D=2 in Table 6 shown in Figure 10b).

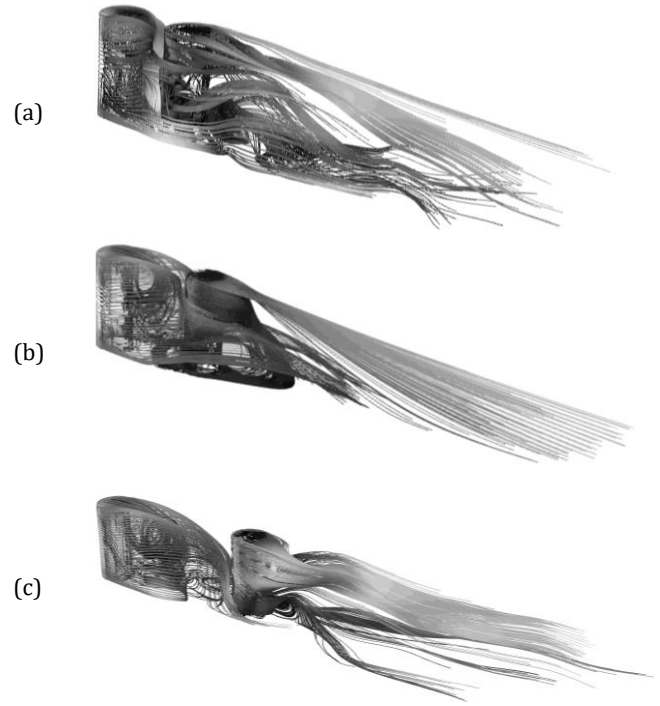

Figure 10. 3D view of horseshoe, Kármán and tip vortex streamlines for (a) S/D=1, (b) S/D=2, (c) S/D=4.

In Figure 11, the cross-sections of the flow field in the xz-plane are presented, depicting the flow patterns for (a) S/D=4, (b) S/D=2, and (c) S/D=1. As shown in Type 6 in Table 6, there is a recirculation zone between the cylinders caused by downwash effect. The flow that accelerates and rises over the upstream cylinder is directed downwards by the downwash effect. Part of the flow separates and creates a recirculation region between the two cylinders, while the other part continues to flow over the downstream cylinder. When the boundary layer formations on the free end surfaces are examined, all three cases display clear boundary layer formations in the upstream cylinder (Type 5 in Table 6).

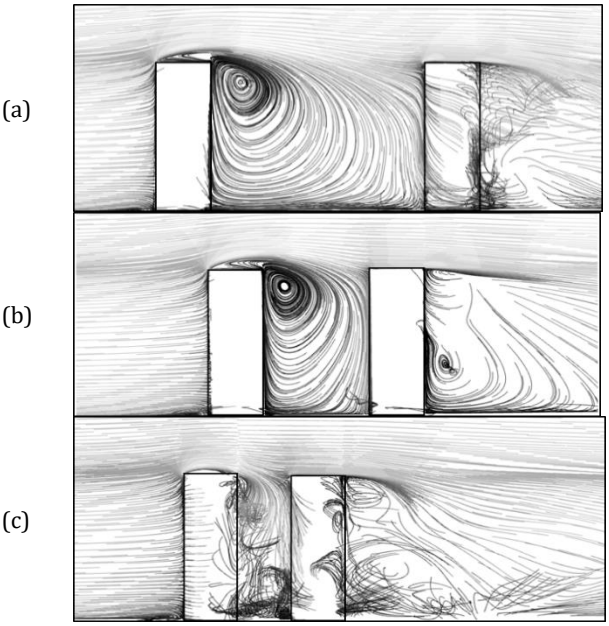

Figure 11. The fluid flow streamlines along the center (*xz)* plane for (a) S/D=4, (b) S/D=2, and (c) S/D=1

Trailing vortex streamlines for S/D=1 are shown in Figure 12. The flow leaving the upstream cylinder sweeps the free end of the downstream cylinder and prevents the formation of a distinct boundary layer above the downstream cylinder. As

S/D is increased, the recirculation zone creates large sweeping effects on the front and free end surfaces of the downstream cylinder. The flow passed the downstream cylinder is affected by downwash that reduces the vertical extend (Type 6, S/D=1 in Table 6 as shown in Figure 12).

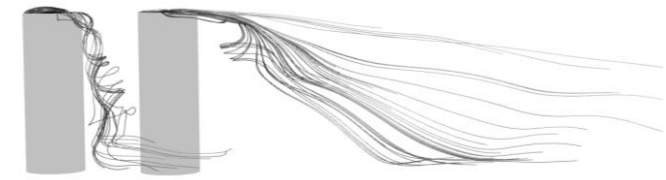

Figure 12. Trailing vortex streamlines for S/D=1.

Finally, a part of the flow tends to rise due to the interaction with the horseshoe separated from the cylinders and the recirculation zones formed behind the cylinders. Table 6 schematizes the rising movement of this flow, called Upwash, for all conditions (Type 7 in Table 6).

Heat Transfer Characteristics

Convection heat transfer from a solid surface to a free stream is quantified by the dimensionless Nusselt number. Especially in the case of surface-mounted tandem finite cylinders, the heat transfer depends mainly on the arrangement and boundary conditions of cylinders. Due to the flow field's shedding and swirling structure, the heat transfer process is unsteady. The numerical results depict instantaneous changes. Once the flow regime had settled, the time-averaged flow and heat transfer quantities were analyzed. The numerical simulation was carried out for four thermal boundary condition scenarios (see Table 1). The time-averaged C_D and time-averaged mean Nusselt numbers were calculated for each scenario, and the results are presented in Table 7.

Table 7. Time averaged mean C_D and Nusselt numbers for all cases.

Cases	Drag Coefficient (C_D)	
	Upstream Cylinder	Downstream Cylinder
Case 1 – S/D =1	0.802	0.211
Case 2 – S/D =1	0.803	0.205
Case 3 – S/D =1	0.813	0.209
Case 4 – S/D =1	0.803	0.219
Case 1 – S/D =2	0.698	0.104
Case 2 – S/D =2	0.698	0.104
Case 3 – S/D =2	0.698	0.104
Case 4 – S/D =2	0.698	0.104
Case 1 – S/D =4	0.703	0.385
Case 2 – S/D =4	0.703	0.387
Case 3 – S/D =4	0.703	0.386
Case 4 – S/D =4	0.703	0.386
Cases	Nusselt Number	
	Upstream Cylinder	Downstream Cylinder
Case 1 – S/D =1	-	-
Case 2 – S/D =1	-	102.52
Case 3 – S/D =1	105.04	-
Case 4 – S/D =1	104.56	98.94
Case 1 – S/D =2	-	-
Case 2 – S/D =2	-	92.13
Case 3 – S/D =2	93.01	-
Case 4 – S/D =2	91.75	87.80
Case 1 – S/D =4	-	-
Case 2 – S/D =4	-	105.30
Case 3 – S/D =4	95.77	-
Case 4 – S/D =4	95.06	104.58

The drag coefficients of both cylinders aren't affected by thermal conditions; in some cases, the cylinders are adiabatic or isothermal. The results show that the C_D decreases from S/D=1 to 2 and increases from S/D=2 to 4 due to the flow velocity changes (see Figure 7 and Figure 8). The lowest C_D values are observed in the case of S/D=2 since the flow is symmetrical and does not shed. Increasing or decreasing the spacing between the cylinders causes an increase in C_D by increasing flow velocity and complex recirculation zones. In the S/D=1, the closest position, there is a chaotic flow field between cylinders (see Figure 11c). Additionally, a high-velocity flow strikes the surfaces of the cylinders over and between them. Therefore, the C_D value in the upstream cylinder for S/D=1 is the highest in all cases. In S/D=4, the farthest position, the upstream cylinder gets away from the tandem structure, and the C_D value decreases. The downstream cylinder has the highest C_D value compared to other arrangements due to its position far from the upstream cylinder wake.

Regarding heat transfer, the behavior of the Nusselt number is similar to the C_D because it is directly related to the flow field. In Case 4, both cylinders are isothermal. The mean Nusselt number of the upstream cylinder decreased by 13.9% from S/D=1 to 2 and increased by 3.6% from S/D=2 to 4. While the downstream cylinder's mean Nusselt number decreased by 12.6% from S/D=1 to 2, it increased by 19.1% from S/D=2 to 4. A similar situation exists in other cases. For example, in Case 3, the mean Nusselt number in the upstream cylinder decreased from S/D=1 to 2 and increased from S/D=2 to 4. It is caused by the turbulent flow character change in S/D from 1 to 2 and 2 to 4 showed in Table 6.

In the flow field, the effect of the downstream cylinder on the upstream cylinder is limited. When the mean Nusselt numbers of the downstream cylinder in Case 3 and Case 4 are compared, it is seen that the thermal boundary type (isothermal or adiabatic, see Table 1) of the downstream cylinder does not affect the mean Nusselt number of the upstream cylinder. For S/D=1, 2, and 4, the mean Nusselt numbers in Case 3 differ from the mean Nusselt numbers in Case 4 by 0.4%, 1.3%, and 0.7%, respectively.

The boundary condition imposed on the upstream cylinder affects the mean Nusselt number of the downstream cylinder. For every S/D, the time-averaged mean Nusselt numbers in Case 2 are greater than in Case 4. Because when the upstream cylinder is adiabatic, the mean Nusselt number is higher because the downstream cylinder encounters the cold fluid. The time-averaged Nusselt numbers in the downstream cylinder in Case 2 and Case 4 are 3.6%, 4.9%, and 0.6% higher for S/D=1, 2, and 4, respectively.

Since the flow structure shows an unsteady structure on the cylinders, regional interpretations are made by examining the time-averaged local Nusselt numbers. The cylinder geometric description for local Nusselt number evaluation is illustrated in Figure 13.

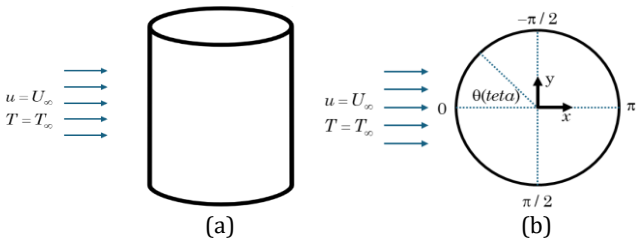

Figure 13. Cylinder geometric description for local Nusselt number evaluation (a) 3D view, (b) top (xy) view.

Figure 14 depicts the contour plots of the time-averaged local Nusselt numbers resulting on the lateral and free end surfaces of the upstream and downstream cylinders for Case-4 and S/D= 4. When the heat transfer around the upstream cylinder is examined in Figure 14a, the front surface region of the upstream cylinder where the flow impinges generally had a higher Nusselt number distribution (θ=±1 and z/D=0 to 3). The zone with maximum Nusselt number values is observed in the circumferential leading edge of the free end (θ=±1 and z/D=3), where flow separation, tip vortices and boundary layer formation occur. The local Nusselt number is also high in the cylinder's lower rear surface (θ=-1.5 to 3.14 and z/D=0 to 1.25), caused by the recirculation zone between the two cylinders.

In Figure 14b, the swirling flow impinges on the front surface of the downstream cylinder. In this case, the local Nusselt number contours are observed to be symmetrical owing to the time-averaged upstream flow. Due to the recirculation zone shown in Figure 11a, the downstream cylinder is swept by the flow, and a high heat transfer region is formed almost on the entire front surface (θ=±2 and z/D=0 to 3). This sweeping flow region, combined with the horseshoe vortex structure coming from the upstream cylinder, affects the front surface of the downstream cylinder. It creates wider high heat transfer regions towards the lower parts (θ=-0.5 to -1.5 and 0.5 to 1.5 and z/D=0.5 to 1.5). Similar to the upstream cylinder, the maximum Nusselt number is observed at the leading edge of the free end surface (θ=±1 and z/D=3). A high local Nusselt number contours are also observed on the rear surface of the downstream cylinder along the center line due to the presence of the recirculation zone in the near wake of the cylinder (θ=-2.5 to -3.14 and 2.5 to 3.14 and z/D=0 to 3).

The flow leaving the upstream cylinder creates a trailing vortex, and this vortex separates into two parts. A part of it joins to the recirculation zone and the other strikes to the free end surface of the downstream cylinder. In Figure 14c, the high heat transfer zone is seen at the leading edge of the free end surface of the upstream cylinder due to the formation of a boundary layer on the leading edge. There is also a local high heat transfer zone in the trailing edge region where the flow is directed towards the recirculation zone with the downwash effect. A high heat transfer region in the downstream cylinder is observed close to the free-end surface center due to the upstream trailing vortex impinging and sweeping it away.

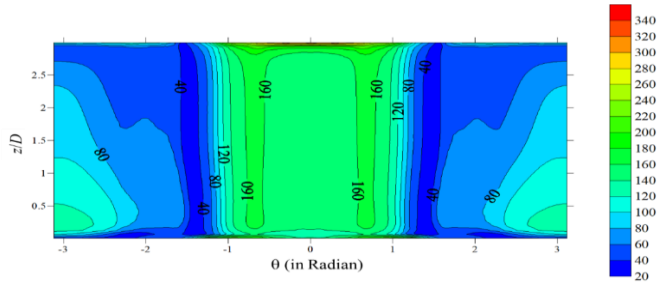

(a)

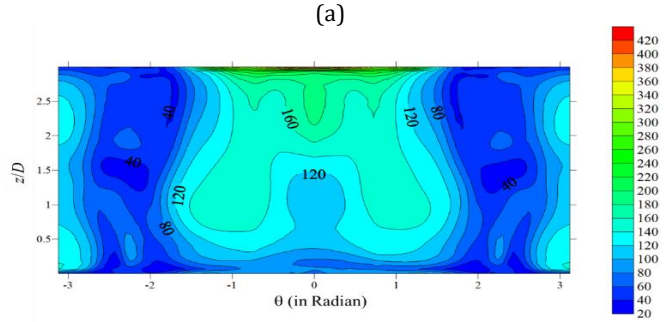

(b)

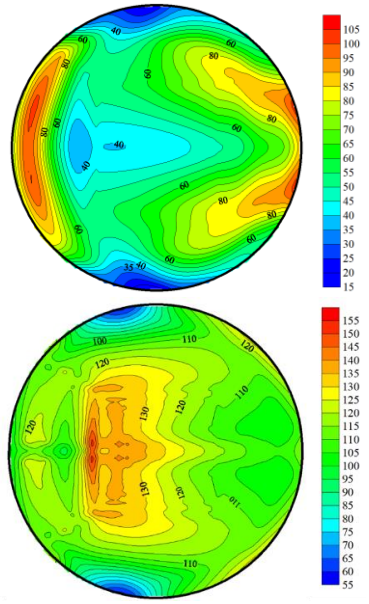

(c)

Figure 14. The time-averaged local Nusselt number distribution (a) upstream and (b) downstream cylinder's lateral surface, (c) Free end surfaces of the upstream (left) and downstream (right) cylinders for Case-4 and S/D= 4.

The local Nusselt number contours of the lateral and free end surfaces of the upstream and downstream cylinders are illustrated in Figure 15 for Case 4 and S/D=2. It can be seen that the front surface of the upstream cylinder has a high heat transfer region over the front surface (θ=±1 and z/D=0-3) (see Fig. 15a). Generally, the local Nusselt number distribution is similar to the upstream cylinder of S/D=4 (see Fig. 14a). The zone with maximum Nusselt number values is observed in the circumferential leading edge of the free end (θ=±1 and z/D=3), where flow separation, tip vortices and boundary layer formation occur. As the distance between the two cylinders decreases, the recirculation region narrows and its center rises (Figure 11b). Therefore, there is a local high heat transfer region slightly lower than S/D=4 on the rear surface of the upstream cylinder (θ=2.5 to 3.14 and z/D=0 to 2.25).

On the downstream cylinder, it is understood that the region of high local Nusselt numbers in the front surface shrinks as the recirculation region between the two cylinders decreases as a result of reducing the distance between the cylinders. As clearly seen in Figure 15b, the high Nusselt number region is located above the front surface middle region (θ=±2 and z/D=1 to 3). Similar to the upstream cylinder, the maximum Nusselt number is observed at the leading edge of the free end surface (θ=±1 and z/D=3). The rear surface of the downstream cylinder slightly affected by the near wake recirculation (θ=2.5 to 3.14). The time-averaged local Nusselt number distribution of free end surfaces of the upstream and downstream cylinders shown in Figure 15c. It is observed that the Nusselt number distribution character is similar to the S/D = 4 and Case 4 arrangement in the upstream cylinder (see Figure 14c). On the downstream cylinder, the highest heat transfer formation is observed at the leading edge of the free end surface. It is caused by the impingement of the trailing vortices comes from upstream cylinder. Generally, a symmetrical and uniformly distributed local Nusselt number contours emerged across the time interval.

The local Nusselt number contours the lateral and free end surfaces of the upstream and downstream cylinders are

illustrated in Figure 16 for Case 4 and S/D=1. The local Nusselt number contour of the upstream cylinder's front surface of S/D=1 is similar to S/D = 2 and 4 due to the upcoming flow structure similarity. The front surface of the upstream cylinder has a high heat transfer region (θ=±1 and z/D=0-3) (Figure 16a). In addition, the zone with maximum Nusselt number values is observed in the circumferential leading edge of the free end (θ=±1 and z/D=3). Unlike other arrangements, a chaotic flow field occurs between the two cylinders (Fig. 11c), creating a high Nusselt number zone on the rear surface of the upstream cylinder. Higher Nusselt numbers than S/D=2 and 4 are observed on the rear surface of the upstream cylinder (θ=-2 to -3.14 and 2 to 3.14 and z/D=0.5 to 2.75).

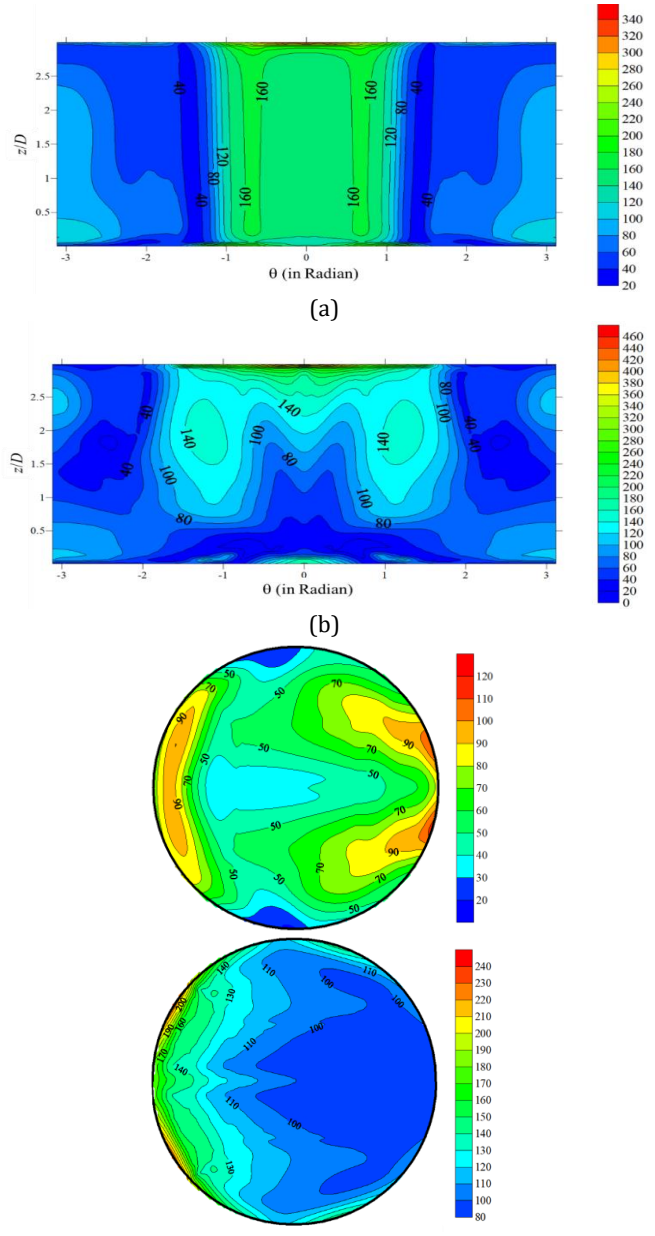

Figure 15. The time-averaged local Nusselt number distribution (a) upstream and (b) downstream cylinder's lateral surface, (c) Free end surfaces of the upstream (left) and downstream (right) cylinders for Case-4 and S/D= 2.

It is understood that a clear recirculation region is not formed as the distance between the cylinders decreases (Figure 11c and Figure 10a). The flow in between becomes more complex and changes the distribution of high heat transfer regions shown in Figure 16b. When the Nusselt number distributions on the lateral surfaces of the downstream cylinder are examined, it is observed that separate Nusselt number islands are formed. The high heat transfer region in the upper part formed by the trailing vortex is located in a higher position compared to the other arrangements (θ=-0.5 to -2 and 0.5 to 2 and z/D=1.25 to 3). In the lower parts of the cylinder, the horseshoe vortex separated from the upstream cylinder interacts with the flow between the two cylinders and forms separated local high heat transfer islands in the lower part of the cylinder (θ=±1.5 and z/D=0 to 1). For lateral surface of the downstream cylinder, the maximum Nusselt number is observed at the leading edge of the free end surface (θ=±1 and z/D=3), similar to the upstream cylinder.

Figure 16c illustrates the time-averaged local Nusselt number contours of the upstream and downstream cylinders' free-end surfaces. Unlike other arrangements, the flow leaving the upstream cylinder immediately dives between the cylinders (Figure 11c). Therefore, the maximum Nusselt number is observed at the trailing edge of the upstream cylinder and the leading edge of the downstream cylinders. A heat transfer trace, an arc-shaped trailing vortex originating from the upstream cylinder, can be seen on the rear cylinder.

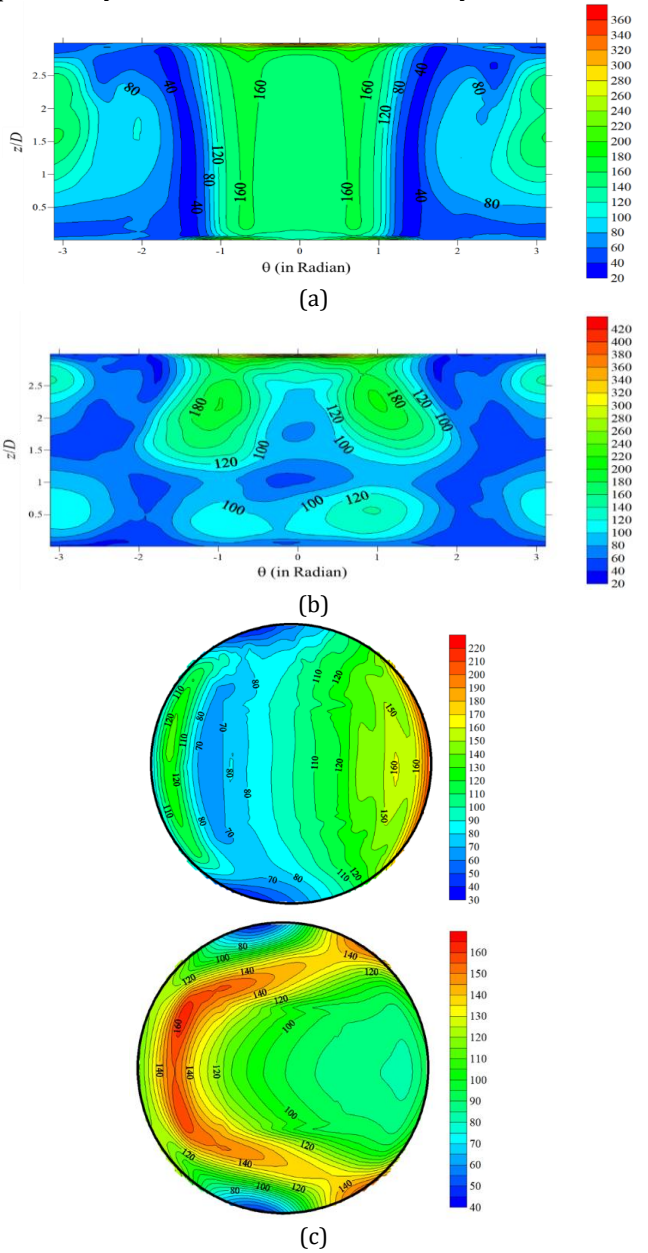

Figure 16. The time-averaged local Nusselt number distribution (a) upstream and (b) downstream cylinder's lateral surface, (c) Free end surfaces of the upstream (left) and downstream (right) cylinders for Case-4 and S/D= 1.

CONCLUSION

The unsteady flow and heat transfer characteristics of two tandem cylinders of finite height (aspect ratio, AR=3) subjected to airflow were numerically investigated. The governing flow and energy equations were solved for the Re=20000 and S/D=1, 2, and 4 arrangements. Furthermore, four distinct thermal boundary conditions were considered for each cylinder configuration. The flow patterns and time-averaged local and mean Nusselt number distributions on the cylinder surfaces were analyzed to elucidate the underlying flow and heat transfer mechanisms.

Flow characteristic results:

- Generally, the upstream cylinder exhibits a higher C_D across all arrangements. For S/D=1, the maximum C_D was observed on the upstream cylinder, which is attributed to the acceleration and a chaotic flow region between the cylinders.
- Kármán street does not develop at S/D=1 case due to irregular vortex shedding. At S/D=2, vortex shedding is significantly damped in the downstream cylinder, and a smooth downwash is observed in the downstream region. At S/D=4, a stable Kármán Street forms, and the flow characteristics insensitive to the thermal boundary conditions.
- Symmetrical flow patterns are generally observed on the upstream cylinder under all conditions. As the spacing between the cylinders decreases, the recirculation zone behind the upstream cylinder becomes increasingly complex, and a three-dimensional (3D) flow structure is evident.
- In all cases, a well-defined boundary layer forms on the free end of the upstream cylinder, but its development is suppressed toward the trailing edge due to the downwash effect.
- The downwash effect is evident in all cases, leading to the formation of recirculation zones between the two cylinders. Furthermore, it inhibits boundary layer development on the free end surfaces of the downstream cylinders.
- Vortex shedding is observed on the downstream cylinders at S/D=1 and 4. In contrast, at S/D=2, a turbulent but symmetrical flow structure is present, which suppresses vortex shedding.

Heat transfer results:

- Generally, regions of high heat transfer are observed on the front surfaces and the leading edges of the free ends of the upstream cylinders.
- The regions of high heat transfer between the cylinders increase in extent from S/D=1 to 4 which is attributed to the gradual expansion of the recirculation zone in this region.
- Generally, localized regions of high local Nusselt numbers are observed on the front surface of the downstream cylinder, primarily due to the recirculation zone and trailing vortex shed by the upstream cylinder.
- Examination of the free end surfaces reveals high local Nusselt number regions at the circumferential leading edges. Furthermore, elevated Nusselt numbers are observed at the trailing edges of the free ends, primarily due to the trailing vortex and the downwash effect, which initiates the recirculation zone. However, the formation of a boundary layer is generally suppressed on the free ends of the downstream cylinders.

In light of the findings, several practical design recommendations can be derived for engineering applications involving tandem finite cylinders.

(i) For optimal heat transfer performance, a spacing ratio of S/D=1 is recommended for the upstream cylinder, where the highest local Nusselt numbers are observed due to intense flow impingement and complex vortex interactions. Conversely, for the downstream cylinder, a larger spacing (S/D=4) yields the best thermal performance, as it enables the formation a stable Kármán vortex street and enhances convective heat transfer.

(ii) The drag coefficient analysis indicates that S/D=2 offers the most favorable aerodynamic balance, with minimal drag resulting from symmetrical flow and reduced vortex shedding intensity making it a suitable choice for applications where both low resistance and moderate heat transfer are desired.

(iii) The thermal boundary conditions of the downstream cylinder influence the upstream cylinder's heat transfer only indirectly, whereas the upstream cylinder's condition significantly affects the downstream performance. Consequently, in designs where the upstream cylinder is adiabatic, the downstream cylinder benefits from enhanced heat transfer due to the cooler incoming flow.

Finally, the detailed classification of flow structures presented in Table 6 can serve as a valuable reference for engineers and researchers to predict flow behavior and thermal performance without conducting full-scale simulations. This study is limited to isothermal tandem cylinders of equal height at Re=20,000, while the effects of varying Reynolds numbers and unequal cylinder heights will be addressed in future work.

ACKNOWLEDGEMENTS

I would like to express my deep appreciation to my superiors at TUSAŞ Engine Industries INC. for allowing me to use technical equipment to conduct this study.

REFERENCES

Alam, M. M., Ullah, Z., Zhu, H., Ji, C., Islam, M., Zeinoddini, M., 2026, Impact of cylinder diameter and spacing on fluid flow, forces, and heat transfer in tandem cylinder configuration. International Journal of Heat and Fluid Flow, vol. 118, 110178. https://doi.org/10.1016/j.ijheatfluidflow.2025.110178

Altaç, Z., Sert, Z., Mahir, N., Timuralp, Ç., 2019, Mixed convection heat transfer from a triangular cylinder subjected to upward cross flow, International Journal of Thermal Sciences, vol. 137, 75-85, https://doi.org/10.1016/j.ijthermalsci.2018.11.010.

Bangga, G., Ashfahani, A., Sugianto, E., Sa'adiyah, D., Putri, T., Jost, E., Lutz, T., 2017, Three-dimensional flow in the vicinity of a circular cylinder mounted to a flat plate at high Reynolds number, AIP Conference Proceedings, 1788, https://doi.org/10.1063/1.4968265.

Çelik, Z., Altaç, Z., 2023, Numerical investigation of two-dimensional unsteady flow and heat transfer from rounded

equilateral isothermal triangular cylinders in cross flow, Ocean Engineering, vol. 269, 113468, https://doi.org/10.1016/j.oceaneng.2022.113468.

Derakhshandeh, J. F., Gharib, N., 2021, Numerical studies of laminar flow over two tandem elliptical cylinders using Ramanujan approximation, Journal of the Brazilian Society of Mechanical Sciences and Engineering, Journal of the Brazilian Society of Mechanical Sciences and Engineering, vol. 43:169, 1-17, https://doi.org/10.1007/s40430-021-02890-0.

Fallah, D. A., Rezazadeh, S., Jalili, H., Raad, M., 2022, Numerical investigation of triangular bluff bodies size effect on heat and mass transfer phenomena: internal flow, Journal of the Brazilian Society of Mechanical Sciences and Engineering, 44:219, 1-18, https://doi.org/10.1007/s40430-022-03526-7.

Freidooni, F., Sohankar, A., Rastan, M., R., Shirani, E., 2021, Flow field around two tandem non-identical-height square buildings via LES, Building and Environment, vol. 201, https://doi.org/10.1016/j.buildenv.2021.107985.

Göktepeli, İ., 2025a, Numerical Investigation of Two-Dimensional Flow past a Normal Flat Plate, Firat University Journal of Experimental and Computational Engineering, Vol. 4 (3), 545-556. https://doi.org/10.62520/fujece.1639083

Göktepeli, İ., 2025b, Drag reduction by the effect of rounded corners for a square cylinder, Physics of Fluids, vol. 36 (9), 094108. https://doi.org/10.1063/5.0228446

Gouidmi, H., Benderradji, R., Beghidja, A., 2019, Numerical study a flow around a heated finite cylinder and mounted vertically on a flat plate, WSEAS Transactions on Heat And Mass Transfer.

He, J., Zhao, W., Wan, D., O, A., 2017, CFD Simulations of flows around finite stubby circular cylinder with free end, Proceedings of the Twenty-seventh International Ocean and Polar Engineering Conference.

Homsi, R., Islam, D., Fatt, Y., Janajreh, I., 2021, Flow dynamics over a heated cylinder subjected to high temperature ratios, Case Studies in Thermal Engineering, vol. 27, https://doi.org/10.1016/j.csite.2021.101357.

Hossain, Md M., Nayeem, M. H. K., Ali, Md A. T., 2021, Numerical study of flow characteristics around rectangular cylinders in tandem, Journal Of Mechanical Engineering, Automation And Control Systems, vol. 2 (1), 36-43, https://doi.org/10.21595/jmeacs.2021.21899.

Kawamura, T., Hiwada, M., Hibino, T., Mabuchi, I., Kumada, M., 1984, Flow around a Finite Circular Cylinder on a Flat Plate : Cylinder height greater than turbulent boundary layer thickness, Bulletin of JSME, vol. 27, no 232-10, https://doi.org/10.1299/jsme1958.27.2142.

Kondo, N., Matsukuma, D., 2005, Numerical simulation for flow around two circular cylinders in tandem, International Journal of Computational Fluid Dynamics, vol. 19, https://doi.org/10.1080/10618560500234345.

Koçak, T. B., 2024, Art Arda Dizili Sonlu Dairesel Silindirlerin Akışkan Akışı ve Isı Transferi İncelemesi, PhD Thesis, Mechanical Engineering Department, Esk. Osmangazi Univ., Eskişehir, Turkey.

Krajnovic, S., 2011, Flow around a tall finite cylinder explored by large eddy simulation, Journal of Fluid Mechanics, vol. 676, https://doi.org/10.1017/S0022112011000450.

Liakos, A., Malamataris, N., A., 2016, Three-Dimensional, Laminar Flow Past a Short, Surface-Mounted Cylinder, American Institute of Aeronautics and Astronautics Journal, https://doi.org/10.2514/1.J054684.

Mahir, N., Altaç, Z., 2008, Numerical investigation of convective heat transfer in unsteady flow past two cylinders in tandem arrangements, International Journal of Heat and Fluid Flow, vol. 29., 1309-1318, https://doi.org/10.1016/j.ijheatfluidflow.2008.05.001.

Menter, F.R., Kuntz, M., Langtry, R., 2003, Ten years of industrial experience with the SST turbulence model, Heat Mass Transf. 4 (2003) 625–632.

Naik, H., Tiwari, S., 2015, Heat transfer and fluid flow charactesistics from finite height circular cylinder mounted on horizontal plane, International Conference on Computational Heat and Mass Transfer, Procedia Engineering, vol. 127, https://doi.org/10.1016/j.proeng.2015.11.428.

Saha, A., K., Biswas, G., Muralidhar, K., 2003, Three-dimensional study of flow past a square cylinder at low Reynolds numbers, International Journal of Heat and Fluid, vol. 24, https://doi.org/10.1016/S0142-727X(02)00208-4.

Sharma, A., Mittal, H., Gairola, A., 2019, Detached-eddy simulation of interference between buildings in tandem arrangement, Journal of Building Engineering, vol. 21, 129-140, https://doi.org/10.1016/j.jobe.2018.10.004.

Sert, Z., 2024, Combined forced and natural convection from a single triangular cylinder, Journal of Thermal Science and Technology, vol. 44 (1), 71-88, https://doi.org/10.47480/isibted.1494043.

Sert, Z., Mahir, N., Altaç, Z., 2024, Numerical investigation of mixed convection from rectangular cylinders subjected to upper cross flow, Numerical Heat Transfer, Part A: Applications 85 (4), 570-591, https://doi.org/10.1080/10407782.2023.2189188.

Sumner, D., 2013, Flow above the free end of a surface-mounted finite-height circular cylinder: A review, Journal of Fluids and Structures, vol. 43, 41-63, https://doi.org/10.1016/j.jfluidstructs.2013.08.007.

Sumner, D., Rostamy, N., Bergstrom, D., J., Bugg, J., D., 2015, Influence of aspect ratio on the flow above the free end of a surface-mounted finite cylinder, International Journal of Heat and Fluid Flow, vol. 56, 290-304, https://doi.org/10.1016/j.ijheatfluidflow.2015.08.005.

Yağmur, S., Dogan, S., Aksoy, M., H., Goktepeli, I., 2020, Turbulence modeling approaches on unsteady flow structures around a semi-circular cylinder, Ocean Engineering, vol. 200, https://doi.org/10.1016/j.oceaneng.2020.107051.

Zafar, F., Alam, M., 2019, Flow structure around and heat transfer from cylinders modified from square to circular, Physics of Fluids, vol. 31, https://doi.org/10.1063/1.5109693.

Zhang, H., Liu, T., Tse, K. T., Gao, H., Zhou, L., 2022, Numerical investigation of the flow past two transversely forced oscillating cylinders in a tandem arrangement, Ocean Engineering, vol. 251, 110757, https://doi.org/10.1016/j.oceaneng.2022.110757.

Zhang, D., Cheng, L., An, H., Draper, S., 2021, Flow around a surface-mounted finite circular cylinder completely submerged within the bottom boundary layer, European Journal of Mechanics / B Fluids 86, 169-197, https://doi.org/10.1016/j.euromechflu.2020.11.011.

Zhang, D., 2017, Comparison of various turbulence models for unsteady flow around a finite circular cylinder at re=20000, Journal of Physics: Conference Series, 910 01202. https://doi.org/10.1088/1742-6596/910/1/012027.

Zhou, Y., Yiu, M., W., 2006, Flow structure, momentum and heat transport in a two-tandem-cylinder wake, Journal of Fluid Mechanics, vol. 548, https://doi.org/10.1017/S002211200500738X.

Zobeyer, H., Baki, A. B. M., Nowrin, S., N., 2021, Interactions between tandem cylinders in an open channel: impact on mean and turbulent flow characteristics, Water, vol. 13, https://doi.org/10.3390/w13131718.